



Deposited via The University of Leeds.

White Rose Research Online URL for this paper:

<https://eprints.whiterose.ac.uk/id/eprint/195455/>

Version: Supplemental Material

Article:

Surawy-Stepney, T, Hogg, AE, Cornford, SL et al. (2023) Episodic dynamic change linked to damage on the Thwaites Glacier Ice Tongue. *Nature Geoscience*, 16. pp. 37-43. ISSN: 1752-0894

<https://doi.org/10.1038/s41561-022-01097-9>

© The Author(s), under exclusive licence to Springer Nature Limited 2023. This version of the article has been accepted for publication, after peer review (when applicable) and is subject to Springer Nature's AM terms of use (<https://www.springernature.com/gp/open-research/policies/accepted-manuscript-terms>), but is not the Version of Record and does not reflect post-acceptance improvements, or any corrections. The Version of Record is available online at: <https://doi.org/10.1038/s41561-022-01097-9>.

Reuse

Items deposited in White Rose Research Online are protected by copyright, with all rights reserved unless indicated otherwise. They may be downloaded and/or printed for private study, or other acts as permitted by national copyright laws. The publisher or other rights holders may allow further reproduction and re-use of the full text version. This is indicated by the licence information on the White Rose Research Online record for the item.

Takedown

If you consider content in White Rose Research Online to be in breach of UK law, please notify us by emailing eprints@whiterose.ac.uk including the URL of the record and the reason for the withdrawal request.

Contents

1	Observed Ice Speed and Error Measurements	2
2	Fracture and Calving Front Measurements	3
2.1	Deep Neural Networks - Background	3
2.2	Network Architecture	3
2.3	Neural Network Fracture Measurement	3
2.3.1	Fracture Detection: Error Estimation and Performance	4
2.4	Neural Network Calving Front Delineation	4
2.4.1	Neural Network Calving Front Error Estimation	5
3	The Temperature Component of Damage	5
4	External Forcing Mechanisms	6
4.1	Ocean Temperature Data	7

1 Observed Ice Speed and Error Measurements

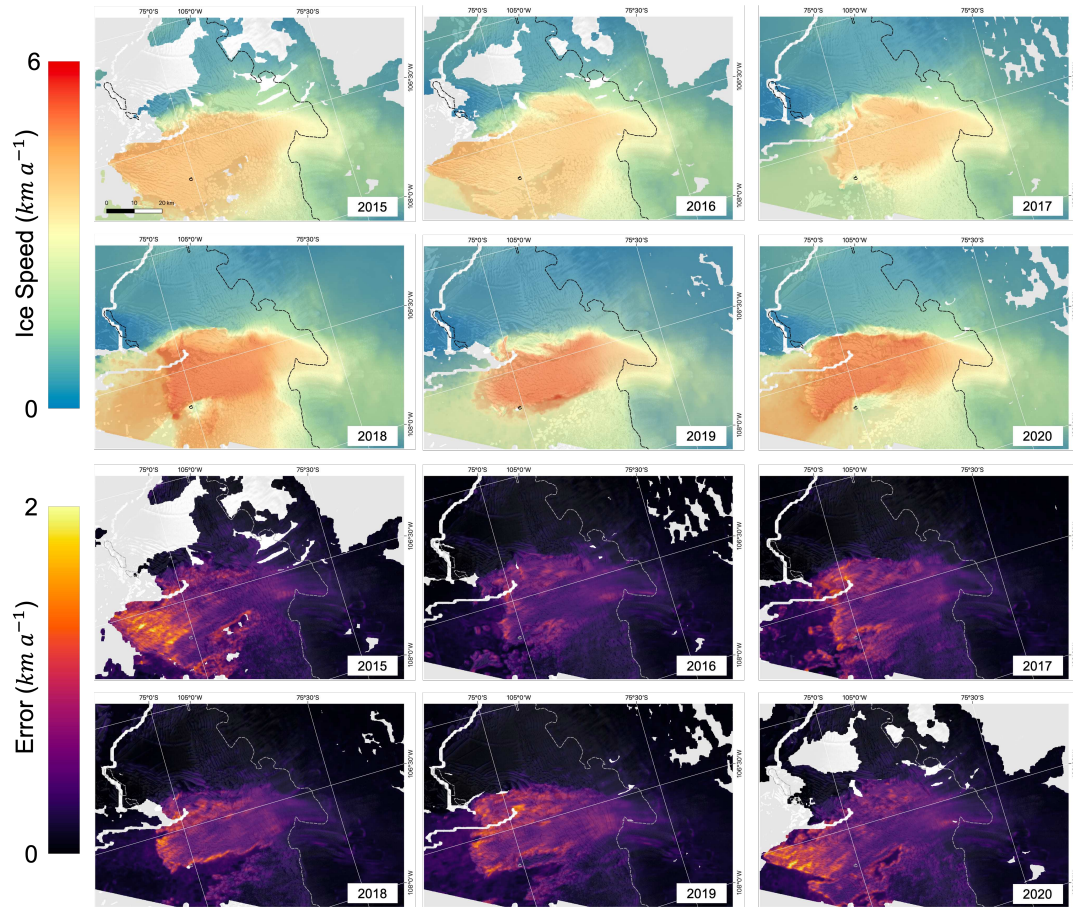


Figure S1: Ice Speed and Error Maps. Annual median mosaics of ice speed (rows 1 and 2) and ice speed error (rows 3 and 4) over TG from 2015 to 2020, as measured using the intensity feature tracking method. The ice speed error is estimated as the reciprocal signal-to-noise ratio of the cross-correlation peak at each feature tracking window, scaled by the local measurement of ice velocity. We define the signal-to-noise ratio as the amplitude of the primary cross-correlation peak divided by the mean of all secondary peaks (as in [1]). Pixels with less than 20% data coverage during the year are excluded from the annual mosaics. The 2011 grounding line location is also shown as the dashed black lines in rows 1 and 2, and the dashed white lines in rows 3 and 4 ([2]).

2 Fracture and Calving Front Measurements

2.1 Deep Neural Networks - Background

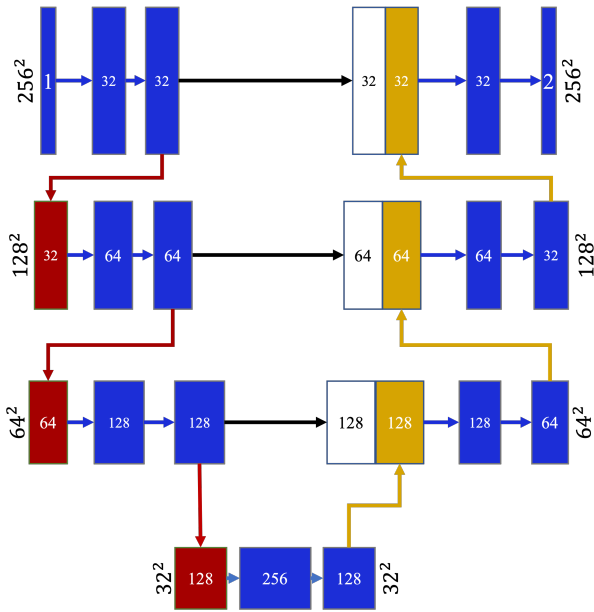


Figure S2: Neural Network Architecture. Network architecture showing 2D convolutions (blue arrows), max-pooling (red arrows) with a kernel size of 3, stride of 2 and padding of 1, skip connections (black arrows), and bilinear up-sampling followed by 2D convolution (gold arrows). Numbers inside boxes indicate the number of channels at each stage, while numbers outside boxes indicate the number of pixels in each channel. All 2D convolutions are of kernel size 3, stride of 1 and padding of 1 except the first two which use kernel size of 7, stride of 1 and padding of 3. The number of trainable parameters in the model totals 534 230.

Over the last decade, deep learning in the field of computer vision has been dominated by convolutional neural networks. These models have been responsible for significant advances in areas such as image classification, segmentation and feature extraction ([3, 4, 5, 6]). Such neural networks operate by applying to the elements x_i of a dataset $\mathcal{X} = \{x_i\}_{i=1}^N$ a series of successive convolutional transformations with trainable parameters θ , separated by non-linear transformations. In a supervised learning regime the output of this series of transformations \hat{y}_i is compared to the desired output - or *target* - $y_i \in \mathcal{Y}$ using a “cost function”, $f : (y_i, \hat{y}_i) \mapsto f(y_i, \hat{y}_i) \in \mathbb{R}$, which defines a distance measure between model outputs and targets. By updating the parameters θ according to the minimisation of the cost function via stochastic gradient descent (where the gradient at each step is calculated only for a subset of the data $b \subset \mathcal{X}$ with cardinality referred to as the “batch size”), the neural network is trained to approximate the desired mapping $m : \mathcal{X} \rightarrow \mathcal{Y}$.

2.2 Network Architecture

The architecture we use (Fig. S2) for both fracture and calving front detection was based on the U-Net ([5]), and is similar to that used by [7] for the segmentation of vegetation from remote sensing imagery. Unlike the original U-Net, we perform bilinear up-sampling followed by 2D convolution in

the decoder section instead of transposed convolution, include batch normalisation after each 2D convolution, dropout with probability 0.1 after each Leaky-ReLU activation, and reduce the network depth considerably. The model was written in Pytorch ([8]) and trained using an Nvidia Tesla K80 GPU.

2.3 Neural Network Fracture Measurement

A large training dataset $(\mathcal{X}, \mathcal{Y})$ is required to train the U-Net to identify surface crevasses on TG in SAR images. Given the scale of the challenge presented by creating such a dataset manually, we opt instead to use a combination of manual annotation, bootstrapping and image augmentation to achieve this. First, we manually delineated the *calving front location* at 50 m spatial resolution in 20 Sentinel-1 interferometric-wideswath mode SAR backscatter images, from 10 glacier locations in Antarctica, ignoring the presence of crevasses in the images. These scenes were selected to represent the realistic variation of surface features seen in SAR images of Antarctica. The images were then tiled into 256×256 pixel patches, before random rigid transformations were applied - preferentially to image patches containing calving fronts. This resulted in 3000 images with associated segmentation maps, 85% of which contained sections of calving front (an example training pair is given in Fig. S3a and b). The neural network was then trained on this calving front dataset using cross entropy loss, Adam optimisation ([9]) with a learning rate of 0.0005, and a batch size of 32. The training was stopped after 9 epochs (44 minutes), before convergence of the network parameters. At this time, the network had become capable of discerning large linear features, including the calving fronts, on which it was trained, and crevasses.

We treat calving fronts as a subset of the set of features corresponding to large, linear textural discontinuities in the backscatter images. This subset is ultimately defined by high-level, semantic features e.g. the identification of sea on one side of the calving front, and glacier ice on the other. U-Net is a hierarchical network in which early layers learn to identify low-level spatial features such as texture and the presence of steep intensity gradients, while higher-level semantic features are learned by deeper layers. Skip connections combine early layers with those towards the end of the decoder section of the network, and enable the network to rapidly reduce the cost function early on in training, by using the activations of the shallow layers to inform its output. At this stage, basic semantic information is provided by the deeper layers, for example constraints on the size and linearity of features. Therefore, early on in training, the network learns to identify the superset of linear features consisting of calving fronts and crevasses.

We then applied this partially trained network to a number of unseen images, identified patches for which the network appeared to have performed well, and added those network outputs and corresponding inputs to the training data set, replacing a random sample of the calving front training images. The network was then retrained with the new data-set before this procedure was repeated. This formed the “bootstrapping” part of the training process.

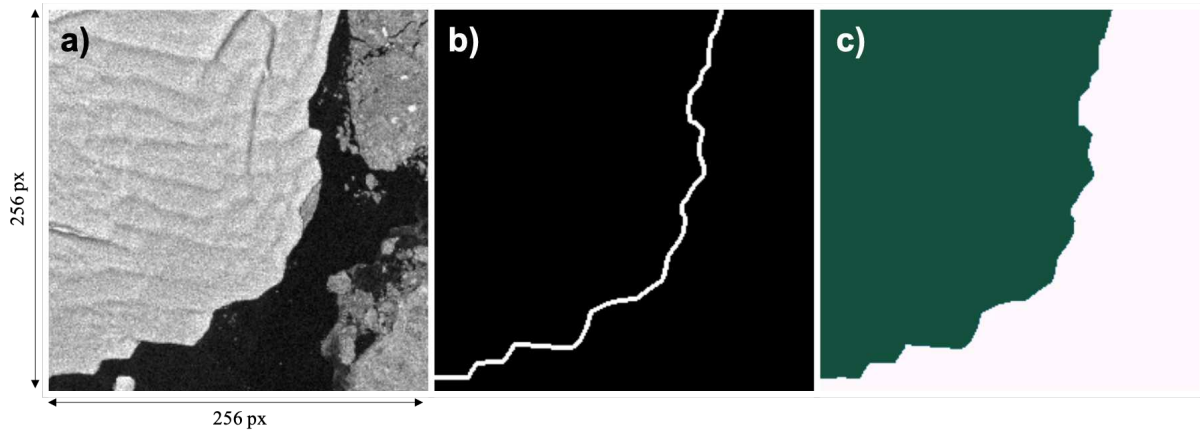


Figure S3: Example Training Data. (a) An example 256×256 -pixel SAR backscatter image included in the training dataset for both fracture and calving fronts. (b) The manually delineated calving front for the corresponding SAR image (a) used during the training of the U-Net for fracture detection, note that no crevasses are identified. (c) The target image corresponding to (a) used to train the network in calving front delineation; this image is segmented into the classes glacier (green) and sea (white).

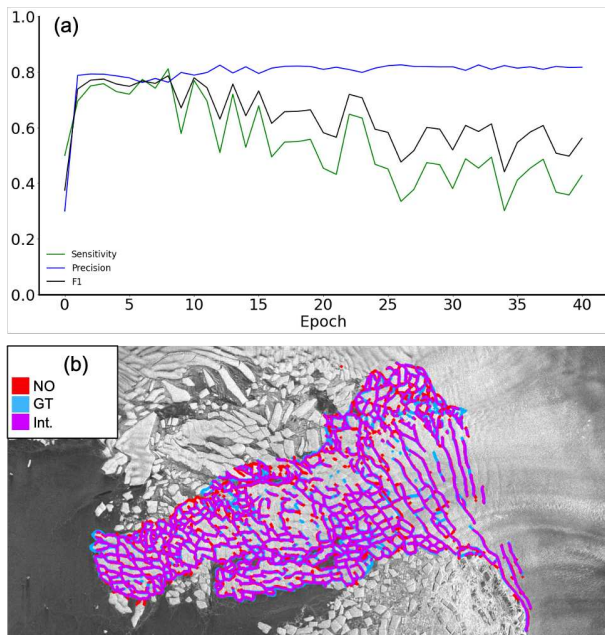


Figure S4: Network Performance and Output. (a) Performance of the neural network as a detector of crevasses after training for 0-40 epochs. (b) Comparison between the network output (red) after 9 epochs and the ground truth (light blue), with the intersection (Int.) between the two data-sets also shown (purple).

2.3.1 Fracture Detection: Error Estimation and Performance

In order to assess the performance of the trained network for the detection of crevasses, the network output after 9 epochs, for a large test image covering the TGIT, was compared to a manually delineated ground truth. The resulting segmentation maps and their intersection clearly shows that there is significant agreement between the ground truth and the network output (Fig. S4b), with both data-sets showing good visual representation of the surface crevasse features visible in the corresponding SAR image. We generated accuracy metrics (Fig. S4a), where *Sensitivity* (S) is the proportion of true frac-

ture locations to be correctly identified by the network, and *precision* (P) is the proportion of fracture locations identified by the network that is true according to the manual annotation. Based on these metrics we define error on the fracture density (ρ_f) in a region to be bounded at the top by $\rho_f \times (2 - S)$ and at the bottom by $\rho_f \times P$. The evolution of the accuracy metrics is shown in Fig. S4b. The sensitivity (green line) is shown to increase to a maximum value of 0.81 after 9 epochs and decrease thereafter, as the network - trained on calving front locations - learns to ignore smaller crevasses. The precision (blue line) increases sharply and plateaus, showing that the network remains successful in the identification of true crevasses. The F1 score ($2PS/(P + S)$) (black line) is also shown, taken as an overall measure of performance. This peaks at 9 epochs, at which point we take the network to be at its optimal efficacy in identifying damage.

2.4 Neural Network Calving Front Delineation

The dataset used in training the U-Net for the segmentation of SAR images into the classes *glacier* and *sea* was split into two parts. The network architecture is the same as that used in the training of the network for crevasse detection, with the calving front target images replaced with binary segmentation maps (Fig. S3a and c). After initial training with this dataset, the model was “tuned” using a smaller training set consisting of 500 patches generated from 5 SAR images of TG, and their manually segmented target images. In both the initial training and the tuning, we used a binary cross-entropy loss function, Adam optimisation with a learning rate of 0.0001, and a batch size of 12. The model training time comprised of 6 hours of initial training and ~ 3 minutes of tuning.

Upon implementation of the trained network, a softmax function was applied to the network output to generate normalised images for each two-channel output. The channels in these normalised images can be interpreted as the probabilities that each pixel corresponds to the classes ‘sea’ and ‘glacier’ respectively. Though this association between a normalised output and a probability is naïve, we make use of it to define a notion of uncertainty in the segmentation (Sect.

2.4.1). As with the fracture measurements, to reconstruct a larger image the 256×256 -pixel patches, which overlap by 128-pixels, are tiled together with a Gaussian weighting away from the centre pixels applied. We extract the calving front location from the probability maps using thresholding and canny edge detection. Unreliable calving front data-points, that don't appear in Fig. 3e of the main text, were identified according to the procedure defined in the methods.

2.4.1 Neural Network Calving Front Error Estimation

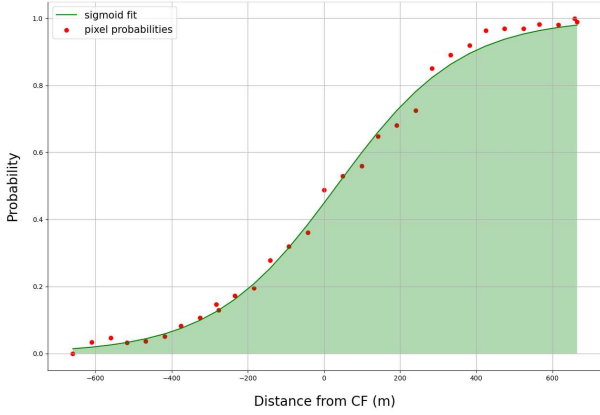


Figure S5: Sigmoid fit to the probabilities that a pixel corresponds to the class ‘glacier’ for pixels close to the calving front along an example measuring line.

We use probability maps, which represent the likelihood that each pixel in the input image is ‘glacier’ (P_g) or ‘sea’ (P_s), to calculate an uncertainty in the calving front position. If we define a transect $c(t)$ along which we measure the distance to the calving front, with $t_0 = 0$ in the sea, and $t_1 = 1$ upstream of the calving front, we can define the probability that each point along that line corresponds to glacier $p_g(t)$. If the value of t corresponds to a true point on the calving front (t_{cf}), then we can denote the probability that each point on the transect corresponds to a point on the calving front as $P_{cf}(t = t_{cf})$. This allows for the following correspondence: $p_g(t) = P_{cf}(t > t_{cf})$. Therefore, if we take $(t_0, t_1) \mapsto (-\infty, +\infty)$, we can view $p_g(t)$ as the cumulative probability distribution of $P_{cf}(t = t_{cf})$ (Fig. S5). A cross-section through P_g approximates a sigmoid function near the calving front, which we can express using parameters μ and σ as:

$$p_g(t) = \frac{1}{1 + e^{-\frac{t-\mu}{q\sigma}}} \quad (1)$$

where $q = \sqrt{3}/\pi$. Differentiating this, we find that $P_{cf}(t = t_{cf})$ follows a logistic distribution with mean μ and standard deviation σ .

Hence, by fitting a sigmoid curve ($s(t; \mu, \sigma)$) to the probabilities that pixels in a cross section of an image P_g , defined by the line $c(t)$, we can estimate the uncertainty in our measured calving front position along that line, namely: σ .

3 The Temperature Component of Damage

The rate factor $A(T)$, in Glen’s flow law depends exponentially on temperature. The effective viscosity of ice, η , defined through $\tau_{ij} = \eta \dot{\epsilon}_{ij}$, can be written

$$\eta = A(T)^{-1} \tau_{II}^{1-n}, \quad (2)$$

where $\tau_{II} = (\tau_{ij}\tau_{ij})^{1/2}$ is the second invariant of the deviatoric stress tensor. Hence, the effective viscosity is strongly temperature dependent as well. Using Hooke’s modification to the Arrhenius relation for $A(T)$ ([10]), we find, at constant stress, and at temperature T , that for a small fluctuation in temperature δT :

$$\frac{\delta \eta}{\eta} = - \left(\frac{Q}{RT^2} + \frac{3Ck}{(T_0 - T)^{k+1}} \right) \delta T, \quad (3)$$

where Q is the activation energy for creep, R is the universal gas constant, $T_0 = 273.39$ K, $C = 0.16612$ K^k is the flow rate factor, and $k = 1.17$. The model inversions undertaken in this study assume a constant temperature field $T \equiv T(x, y)$ ([11]) when calculating ϕ , however, clearly inaccuracies in the temperature field that alter the value of η from eq. 2 will cause changes in ϕ to compensate. We argue that the temperature field is accurate enough for us to ignore this contribution to ϕ and assume that deviations of ϕ from 1 are dominated by ice fracture.

Warmer temperatures in T will cause η in the model to be smaller than in reality, hence a ϕ greater than unity and a negative value of D . We, therefore, investigate errors in the temperature field by looking at negative damage in the inversion outputs.

In Fig. S6 (a)-(b) we see that there are few areas of negative damage, with negative values anyway close to zero. Using the distribution of negative damage values (Fig. S6 (b)), we define a rough error on ϕ induced by errors in the temperature field of $\Delta D \sim 0.05$. We also see, in Fig. S6 (c) that, for a such an error in the effective viscosity, the temperature field would have to be accurate to ~ 2 K, showing that T is likely to be a very good representation of the temperatures in this region of the WAIS.

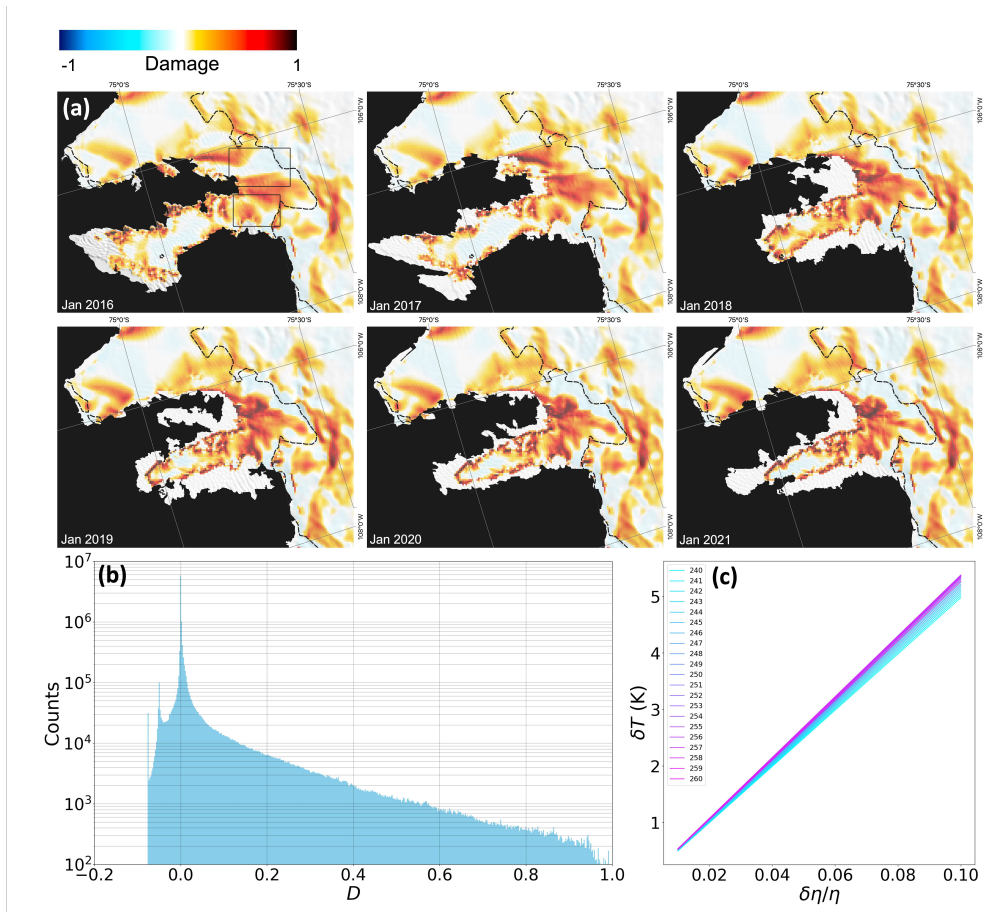


Figure S6: Distribution of D over the TG terminus. (a) shows a reproduction of figure 4 with negative values of damage also shown in blue. The MEASUREs grounding line is shown as the dashed black line [2]. (b) the distribution of damage values over the whole domain and timeseries. (c) temperature fluctuations corresponding to changes in the effective viscosity in the linear regime, using eq. 3, for values of T between 240 and 260 K.

4 External Forcing Mechanisms

In the discussion of the main text, we make clear that external influences beyond the interplay between fracture development and dynamic change are likely required to explain the observations. Here, we briefly discuss such forcing.

Environmental forcing mechanisms known to impact the West Antarctic Ice Sheet include incursions of warm ocean water onto the continental shelf ([12, 13, 14]) or increased discharge of meltwater through the sub-glacial drainage system ([15, 16, 17, 18]), both of which can drive higher rates of basal melt and lead to dynamic speedup. The known decadal variability in ocean forcing in the ASE ([19]) has likely been responsible for past dynamic events and structural changes on the ice tongue ([20, 21]) and will continue to have an influence today. Examination of conductivity-temperature-depth (CTD) casts in the region ([22]) suggest that ocean temperatures in the 400 – 600 m depth range were 0.25 – 0.5 °C warmer in 2019 than in 2014 (Fig. S7).

The absence of detailed knowledge on ocean temperature and circulation during the first ice dynamic episode makes it difficult to robustly link these observations. However, the strong El Niño event in 2016 ([23]) could plausibly have increased oceanic heat delivery to the TGIT during 2017 and

may therefore have played a role in the 2017–2018 acceleration episode and the continued deterioration of TGIT.

Increased sub-glacial discharge is caused by the drainage of sub-glacial lakes, and satellite observations show that two large sub-glacial lakes in the Thwaites catchment drained in March 2017 ([16]). These results indicate that the drainage events led to the filling of a downstream lake rather than routing water to the ice margin, which would seemingly preclude an influence of these lakes on TGIT dynamics. However, given the temporal coincidence of these events we do not rule out a potential link between the drainage event and the acceleration of TGIT.

Surface melting is not thought to play a significant role in Antarctic ice mass loss ([24]), however, observations in Greenland show that surface meltwater penetration to the bed can cause large and rapid speed variations ([25]). Despite observing a decrease in backscatter signal throughout the summer of 2018/19, we found no evidence of supra-glacial melt ponds, but further work is required to understand if surface melt processes were linked to the observed dynamic ice speedup on TG.

Sea ice can act to inhibit iceberg calving even in unconfined Antarctic ice shelves via the bonding of small peripheral icebergs, and by attenuating ocean swell and reducing

the associated ice-shelf flexure ([26]). A visual analysis of SAR backscatter images shows that sea ice retreated beyond the northern-most part of the TGIT in November 2016, and did not fully reform before July 2017 after the large calving events in March and June of that year, indicating that such a process contributed to the structural decline of the TGIT ([21]). Further analysis of SAR images over the full 6-year study period shows that the period of deceleration coincided with an almost complete removal of sea-ice cover in the ocean around TG in January to March 2019, before the return of sea-ice cover prior to the second period of acceleration. This indicates that, although it is responsible for maintaining the structural integrity of the northern sections of the TGIT, sea ice may not always play a decisive role in regulating the speed of the TGIT. Future studies are required to make observations of sea ice thickness in the ice shelf peripheral region, so that the buttressing strength of 1–5 m thick sea ice against the flow of the 300 m thick shelf ice can be quantitatively determined.

4.1 Ocean Temperature Data

To evaluate the possible effect of changing ocean conditions on the stability of TGIT, we examined conductivity, temperature, depth (CTD) profiles acquired near the TGIT in 2014 and 2019. The CTD profiles are from the Ocean2ice iSTAR cruise in 2014 (available at: <http://www.bodc.ac.uk/>) and from the 2019 Nathaniel B. Palmer cruise (available at: <https://doi.pangaea.de/10.1594/PANGAEA.860066>; [27]). All profiles were acquired within 60 km of the TGIT, but the majority of profiles were acquired within 30 km. These profiles (Fig. S7) show that water column temperature in the 400–600 m depth range was approximately 0.25–0.5 °C warmer in 2019 compared to 2014. This difference in temperature was consistent - 85% of the profiles acquired in 2019 were warmer than the 2014 average in the 400–600 m depth range - implying a sustained increase in oceanic heat delivery to the TGIT in 2019 compared to 2014.

Acknowledgements. The LaTeX template used for this document was adapted from that of the European Mathematical Society, licenced under Creative Commons CC BY 4.0.

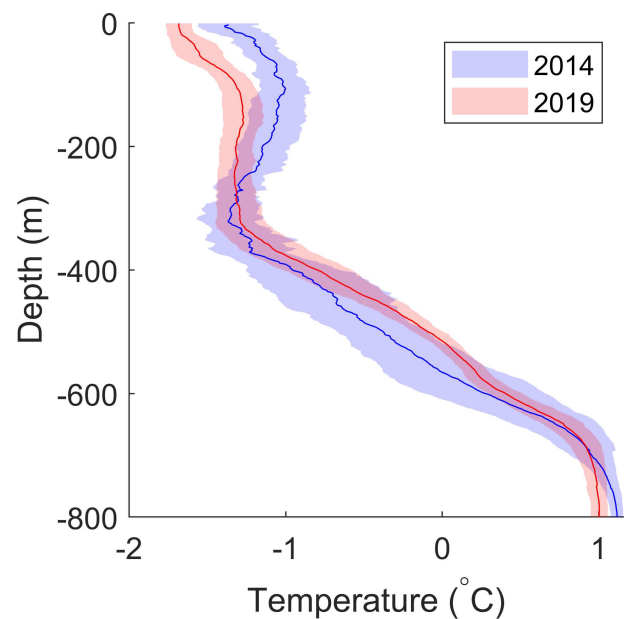


Figure S7: CTD profiles acquired close to the TGIT in 2014 (blue) and 2019 (red). Shaded areas indicate the standard deviation of water column temperature from all profiles acquired within 50 km of the TGIT in each year.

References

- [1] de Lange, R., Luckman, A. & Murray, T. Improvement of satellite radar feature tracking for ice velocity derivation by spatial frequency filtering. *IEEE Transactions on Geoscience and Remote Sensing* **45** (7), 2309–2318 (2007).
- [2] Rignot, E., Mouginot, J. & Scheuchl, B. Measures antarctic grounding line from differential satellite radar interferometry, version 2 (2016). Boulder, Colorado USA. NASA National Snow and Ice Data Center Distributed Active Archive Center. doi: <https://doi.org/10.5067/IKBWW4RYHF1Q>. Accessed 15/01/2021.
- [3] Krizhevsky, A., Sutskever, I. & Hinton, G. E. Imagenet classification with deep convolutional neural networks. *Advances in neural information processing systems* **25**, 1097–1105 (2012).
- [4] Long, J., Shelhamer, E. & Darrell, T. Fully convolutional networks for semantic segmentation (2014). URL <https://arxiv.org/abs/1411.4038>.
- [5] Ronneberger, O., Fischer, P. & Brox, T. U-net: Convolutional networks for biomedical image segmentation (2015). 1505.04597.
- [6] Szegedy, C. *et al.* Going deeper with convolutions (2014). URL <https://arxiv.org/abs/1409.4842>.
- [7] Kattenborn, T., Eichel, J. & Fassnacht, F. E. Convolutional neural networks enable efficient, accurate and fine-grained segmentation of plant species and communities from high-resolution uav imagery. *Scientific reports* **9** (1), 1–9 (2019).
- [8] Paszke, A. *et al.* Pytorch: An imperative style, high-performance deep learning library (2019). URL <https://arxiv.org/abs/1912.01703>.

- [9] Kingma, D. P. & Ba, J. Adam: A method for stochastic optimization. *arXiv preprint arXiv:1412.6980* (2014) .
- [10] LeB. Hooke, R. Flow law for polycrystalline ice in glaciers: comparison of theoretical predictions, laboratory data, and field measurements. *Reviews of Geophysics* **19** (4), 664–672 (1981) .
- [11] Seroussi, H. *et al.* initmip-antarctica: an ice sheet model initialization experiment of ismip6. *The Cryosphere* **13** (5), 1441–1471 (2019) .
- [12] Jacobs, S. S., Jenkins, A., Giulivi, C. F. & Dutrieux, P. Stronger ocean circulation and increased melting under pine island glacier ice shelf. *Nature Geoscience* **4** (8), 519–523 (2011) .
- [13] Jenkins, A. *et al.* West antarctic ice sheet retreat in the amundsen sea driven by decadal oceanic variability. *Nature Geoscience* **11** (10), 733–738 (2018) .
- [14] Dutrieux, P. *et al.* Strong sensitivity of pine island ice-shelf melting to climatic variability. *Science* **343** (6167), 174–178 (2014) .
- [15] Schroeder, D. M., Blankenship, D. D. & Young, D. A. Evidence for a water system transition beneath thwaites glacier, west antarctica. *Proceedings of the National Academy of Sciences* **110** (30), 12225–12228 (2013). URL <https://www.pnas.org/content/110/30/12225>. <https://doi.org/10.1073/pnas.1302828110> .
- [16] Malczyk, G., Gourmelen, N., Goldberg, D., Wuite, J. & Nagler, T. Repeat subglacial lake drainage and filling beneath thwaites glacier. *Geophysical Research Letters* **47** (23), e2020GL089658 (2020) .
- [17] Siegfried, M. R., Fricker, H. A., Carter, S. P. & Tulaczyk, S. Episodic ice velocity fluctuations triggered by a subglacial flood in west antarctica. *Geophysical Research Letters* **43** (6), 2640–2648 (2016) .
- [18] Selley, H. L. *et al.* Widespread increase in dynamic imbalance in the getz region of antarctica from 1994 to 2018. *Nature Communications* **12** (1), 1133 (2021). URL <https://doi.org/10.1038/s41467-021-21321-1>. <https://doi.org/10.1038/s41467-021-21321-1> .
- [19] Jenkins, A. *et al.* Decadal ocean forcing and antarctic ice sheet response: Lessons from the amundsen sea. *Oceanography* **29** (4), 106–117 (2016) .
- [20] Mouginot, J., Rignot, E. & Scheuchl, B. Sustained increase in ice discharge from the amundsen sea embayment, west antarctica, from 1973 to 2013. *Geophysical Research Letters* **41** (5), 1576–1584 (2014) .
- [21] Miles, B. W. J. *et al.* Intermittent structural weakening and acceleration of the thwaites glacier tongue between 2000 and 2018. *Journal of Glaciology* **66** (257), 485–495 (2020). <https://doi.org/10.1017/jog.2020.20> .
- [22] Wählin, A. *et al.* Pathways and modification of warm water flowing beneath thwaites ice shelf, west antarctica. *Science Advances* **7** (15), eabd7254 (2021) .
- [23] Paolo, F. *et al.* Response of pacific-sector antarctic ice shelves to the el niño/southern oscillation. *Nature geoscience* **11** (2), 121–126 (2018) .
- [24] Slater, T. *et al.* Earth’s ice imbalance. *The Cryosphere* **15** (1), 233–246 (2021) .
- [25] Davison, B. J., Sole, A. J., Livingstone, S. J., Cowton, T. R. & Nienow, P. W. The influence of hydrology on the dynamics of land-terminating sectors of the greenland ice sheet. *Frontiers in Earth Science* **7**, 10 (2019) .
- [26] Massom, R. A. *et al.* Antarctic ice shelf disintegration triggered by sea ice loss and ocean swell. *Nature* **558** (7710), 383–389 (2018) .
- [27] Wählin, A. K. *et al.* Pathways and modification of warm water flowing beneath thwaites ice shelf, west antarctica. *Science Advances* **7** (15) (2021). URL <https://advances.sciencemag.org/content/7/15/eabd7254>. <https://doi.org/10.1126/sciadv.abd7254> .